

## Review

# Advances in Imaging Techniques and Genetically Encoded Probes for Photoacoustic Imaging

Chengbo Liu<sup>1,2</sup>, Xiaojing Gong<sup>1</sup>, Riqiang Lin<sup>1</sup>, Feng Liu<sup>1</sup>, Jingqin Chen<sup>1</sup>, Zhiyong Wang<sup>1</sup>, Liang Song<sup>1,2</sup>, Jun Chu<sup>1</sup>

1. Research Laboratory for Biomedical Optics and Molecular Imaging, Institute of Biomedical and Health Engineering, Shenzhen Institutes of Advanced Technology, Chinese Academy of Sciences, Shenzhen 518055, China;
2. Beijing Center for Mathematics and Information Interdisciplinary Sciences (BCMIIS), Beijing 100048, China.

 Corresponding authors: Liang Song (liang.song@siat.ac.cn) or Jun Chu (jun.chu@siat.ac.cn) Tel: +86-755-86392264.

© Ivyspring International Publisher. Reproduction is permitted for personal, noncommercial use, provided that the article is in whole, unmodified, and properly cited. See <http://ivyspring.com/terms> for terms and conditions.

Received: 2016.04.18; Accepted: 2016.05.31; Published: 2016.10.07

## Abstract

Photoacoustic (PA) imaging is a rapidly emerging biomedical imaging modality that is capable of visualizing cellular and molecular functions with high detection sensitivity and spatial resolution in deep tissue. Great efforts and progress have been made on the development of various PA imaging technologies with improved resolution and sensitivity over the past two decades. Various PA probes with high contrast have also been extensively developed, with many important biomedical applications. In comparison with chemical dyes and nanoparticles, genetically encoded probes offer easier labeling of defined cells within tissues or proteins of interest within a cell, have higher stability *in vivo*, and eliminate the need for delivery of exogenous substances. Genetically encoded probes have thus attracted increasing attention from researchers in engineering and biomedicine. In this review, we aim to provide an overview of the existing PA imaging technologies and genetically encoded PA probes, and describe further improvements in PA imaging techniques and the near-infrared photochromic protein BphPI, the most sensitive genetically encoded probe thus far, as well as the potential biomedical applications of BphPI-based PA imaging *in vivo*.

Key words: Molecular Imaging, Photoacoustic Imaging, Photoacoustic Probe, Reporter Gene, Genetically Encoded Probe, Photoswitchable Protein.

## 1. Introduction

Non-invasive monitoring of physiological and pathological processes in deep tissue requires both new imaging techniques and advanced probes [1]. One emerging method is photoacoustic (PA) tomography, an *in vivo* hybrid imaging technology that uniquely combines the absorption contrast of light with ultrasound resolution [2]. PA imaging relies on the conversion of photon energy into ultrasound waves generated by the thermoelastic expansion of tissue following absorption of short laser pulses [3]. The key advantages of PA imaging include 1) great imaging depth (up to 7 cm) in intact biological tissues [4], thereby breaking through the optical diffusion limit (~1 mm depth in the skin) [5]; 2) highly scalable penetration and spatial resolution [6], enabling

multiscale imaging with a PA probe; 3) no speckle artifacts in PA images [7], in contrast to optical coherence tomography (OCT) and ultrasound imaging; 4) no need for ionizing radiation [6], reducing health hazard. Therefore, PA imaging has become a powerful tool for basic research in life sciences, preclinical applications and drug discovery [2, 8, 9].

In general, there are four types of PA imaging systems [10]: optical-resolution photoacoustic microscopy (OR-PAM), acoustic-resolution photoacoustic microscopy (AR-PAM), optical-resolution photoacoustic computed tomography (OR-PACT), and acoustic-resolution photoacoustic computed tomography (AR-PACT) (Figure 1).

Depending on whether the laser beam or ultrasonic detection is more tightly focused, PA imaging can be divided into OR and AR with different lateral resolution. Based on the number of ultrasound detectors and whether a reconstruction algorithm is used, PA imaging can be classified into PAM and PACT. The sensitivity and resolution of these imaging systems vary depending on their optical excitation and acoustic detection configurations, as well as other design considerations of the system.

PA probes, also referred to PA contrast agents, are critical to determine the sensitivity and specificity of PA imaging [11], and have been used to track specific cell populations within an animal when used alone [12, 13] and visualize specific biochemical processes *in vivo* when engineered into biosensors [14, 15]. An ideal PA probe for deep-tissue imaging should meet the following criteria: strong absorption in the near-infrared (NIR) optical window (650-900 nm), low fluorescence quantum yield (QY), high specificity, easy labeling of specific cells and proteins, easy development of functional biosensors, high photostability *in vivo*, high intracellular stability, no toxicity to mammalian cells, and no need for exogenous substances. Endogenous tissue chromophores, such as hemoglobin and eumelanin, which were widely used as cell markers in earlier studies [16-18], cannot label proteins within a cell, and thus can not be used in PA imaging of the dynamics of proteins of interest apart from hemoglobin *in vivo*.

Moreover, hemoglobin cannot be produced in mammalian cells other than blood cells, limiting its usefulness to only blood vessel-related studies. Chemical dyes and nanoparticles overcome the labeling issues of endogenous chromophores to some extent by coupling cell- or protein-specific peptides or antibodies [19-21]. However, these molecules are not very stable in living cells and are quickly cleared away from the body *in vivo* [22], resulting in a low effective concentration of probes in cells and difficulty in longitudinal imaging. By contrast, genetically encoded probes, particularly NIR probes, meet all the above criteria. More importantly, genetically encoded probes can be easily engineered into biosensors to sense various signaling molecules in cells, making them useful for tracking not only cell fates but also molecular functions *in vivo*.

In the present review, we will first describe two classes of PA imaging technologies with optical or acoustic resolution, including their imaging system setups and corresponding applications, then present and discuss genetically encoded PA probes that have been developed so far. Finally, we will give an outlook for further improvements in PA imaging techniques and genetically encoded probes, with a discussion of important applications made possible using the newly developed near-infrared photochromic protein BphP1-based differential PA imaging technique.

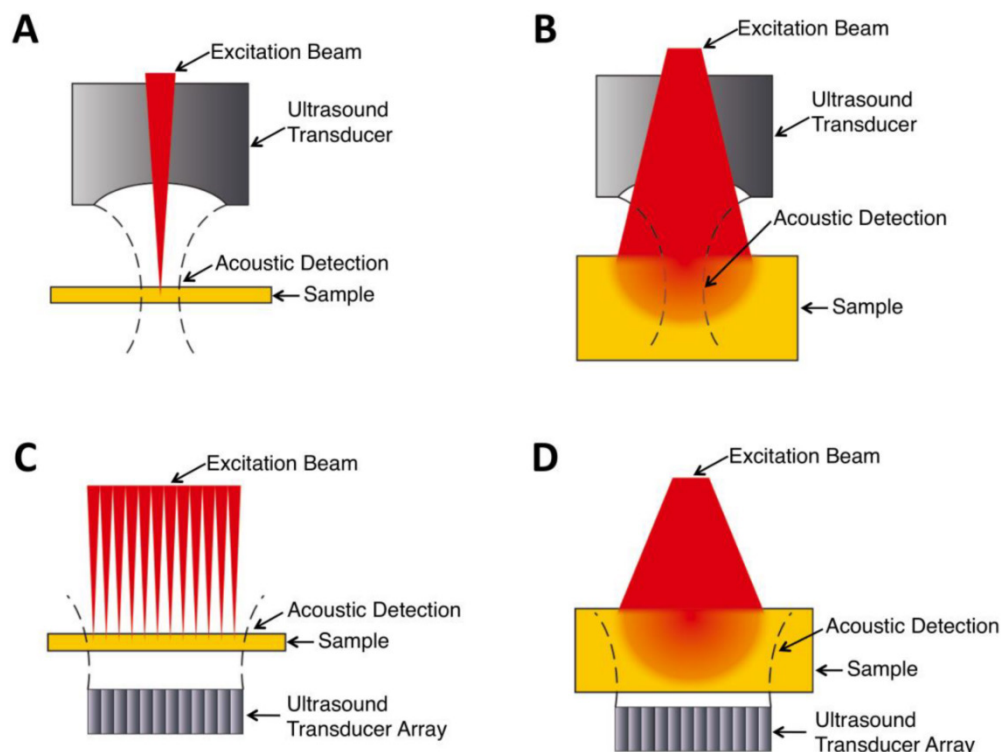


**Figure 1.** Schematic cartoons showing principles of different PA imaging systems. (A) OR-PAM. (B) AR-PAM. (C) OR-PACT. (D) AR-PACT.

## 2. Photoacoustic Imaging Systems

### 2.1 Optical-resolution PA Systems

Within the optical ballistic propagation regime in biological tissue, tight optical focusing can be achieved by restricting the optical excitation to a much more confined area than that of ultrasound detection (Figure 1a, 1c) [23]. Optical-resolution PA systems exploit this tight focusing to obtain a lateral resolution that can be as fine as the optical diffraction limit. The lateral resolution of optical-resolution PA systems can vary from several microns to submicrons (Table 1), depending on the numerical aperture of the optical objective lens [4]. We have reported the development of blind-deconvolution OR-PAM to achieve both fine spatial resolution and extended depth of focus, and further utilized the system to visualize the mouse ear microvasculature *in vivo*

(Figure 2) [24]. By applying an optical objective lens with a much higher numerical aperture and a novel design for PA signal detection, a reflection-mode *in vivo* PA microscope with sub-wavelength lateral resolution was developed that is capable of imaging sub-cellular structure of red blood cells and melanoma cells (Figure 3) [17]. Because OR-PAM typically uses a single-element ultrasonic transducer combined with mechanical or optical scanning to acquire the signal, its imaging speed is relatively slow (Table 1). To increase the imaging speed of OR-PAM, Song *et al.* developed a multifocal OR-PACT with a microlens array for optical illumination in conjunction with an ultrasound array for PA detection [25] (Figure 4A). With this new system, hemoglobin concentration in individual microvessels *in vivo* was monitored at a much higher speed than the single-focus OR-PAM (Figure 4B).

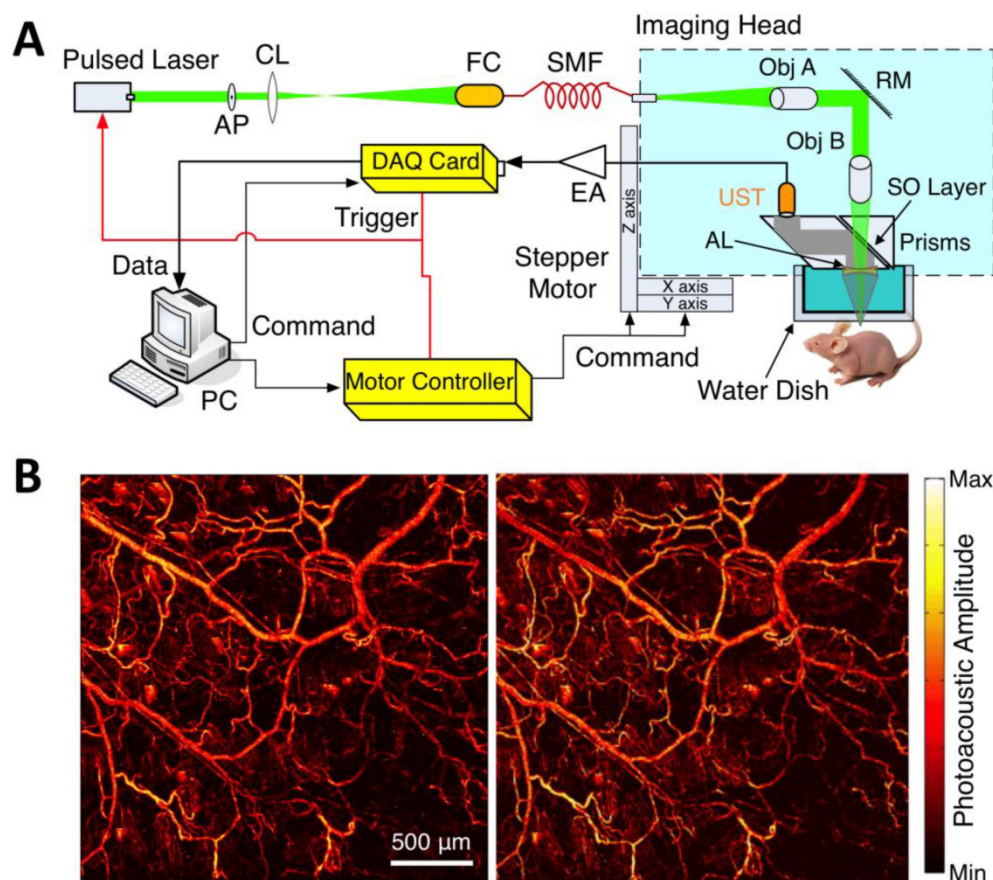


**Figure 2.** OR-PAM imaging of microvasculature in a mouse ear imaged *in vivo*. (A) Schematic diagram of the OR-PAM system. AP, aperture; CL, convex lens; FC, fiber coupler; SMF, single mode fiber; Obj, objective; RM, reflection mirror; UST ultrasonic transducer; AL, acoustic lens; SO, silicone oil; EA, electrical amplifier; DAQ, data acquisition; PC, personal computer. (B) PA images of the microvasculature in a mouse ear with OR-PAM. Left: raw data; right: after blind deconvolution. Figure adapted with permission from [24].

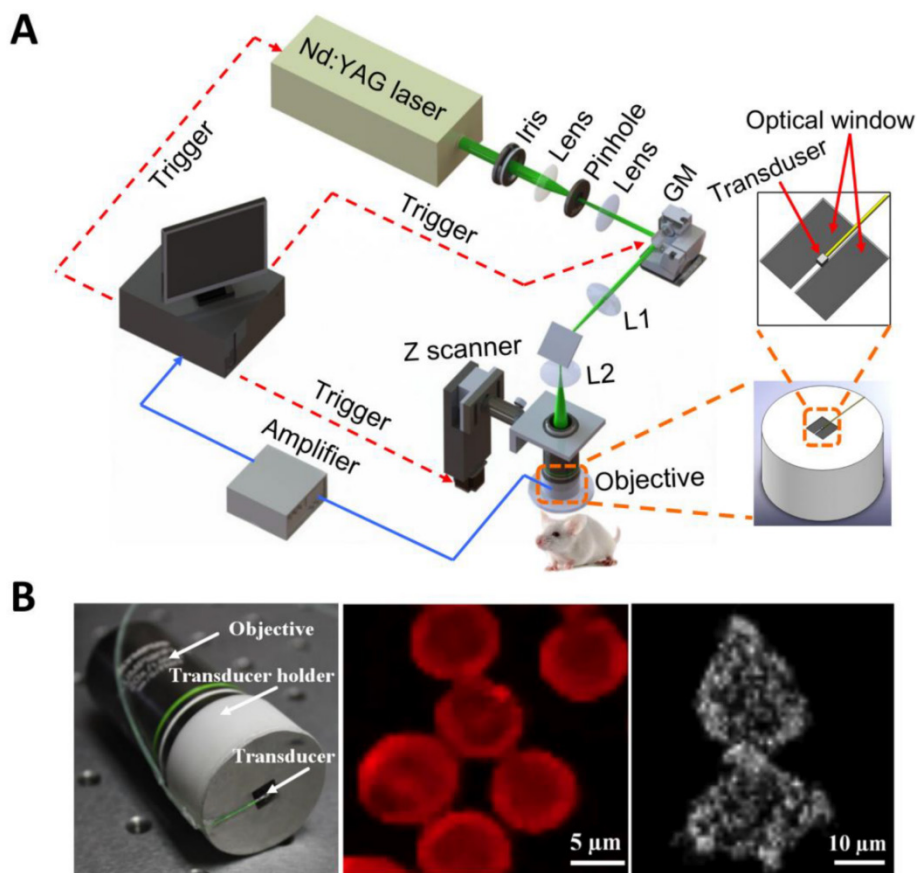


**Figure 3.** Sub-wavelength resolution OR-PAM imaging of single cells *ex vivo*. (A) Schematic diagram of the reflection-mode sub-wavelength resolution PAM system. GM: galvanometer scanner; L1: scan lens; L2: tube lens. (B) Photograph of the PA signal detection probe (left); sub-wavelength resolution PA image of red blood cells (middle) and melanoma cells (right). Figure adapted with permission from [17].

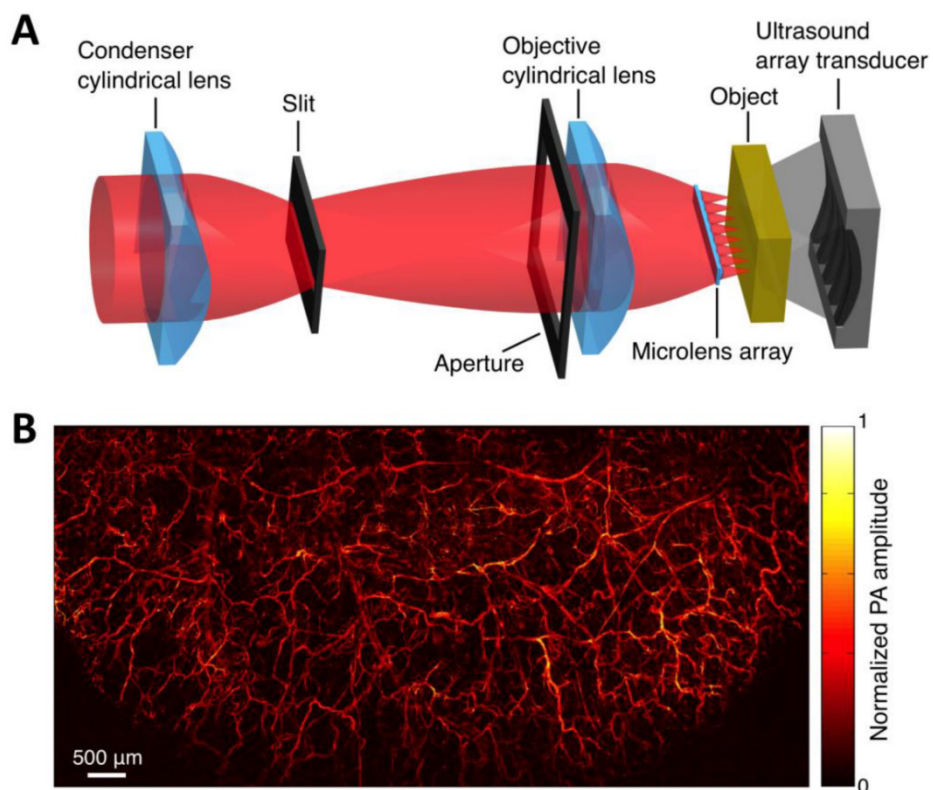


**Figure 4.** Multifocal OR-PACT imaging of microvasculature in a mouse ear. (A) Schematic diagram of the multifocal OR-PACT system. (B) *In vivo* PA MAP (maximum projection amplitude) image of the mouse ear microvasculature. Figure adapted with permission from [25].

**Table 1.** Comparison of different types of PA imaging systems

	OR-PAM	OR-PACT	AR-PAM	AR-PACT
Lateral Resolution	several hundred nms to several $\mu\text{ms}^{\text{a}}$	several $\mu\text{ms}^{\text{a}}$	tens of $\mu\text{ms}$ to hundreds of $\mu\text{ms}^{\text{b}}$	hundreds of $\mu\text{ms}^{\text{c}}$
Axial Resolution <sup>d</sup>	tens of $\mu\text{ms}$	tens of $\mu\text{ms}$	tens of $\mu\text{ms}$ to hundreds of $\mu\text{ms}$	hundreds of $\mu\text{ms}$
Imaging Depth	<1 mm <sup>e</sup>	<1 mm <sup>e</sup>	1-20 mm <sup>f</sup>	10-70 mm <sup>f</sup>
Imaging Speed	tens of minutes	< 1 minute	tens of minutes	< 1 minute
Biomedical Applications	Brain [31, 32] Tumor angiogenesis [35] Oxygen saturation [32, 40] Oxygen metabolism [45] Hemodynamics [48] Subcellular imaging [17, 49]	Brain [33] Blood vessel [25, 36]	Tumor [26, 34] SLNs [37] Brain [41, 42] Whole body [46]	Tumor [1, 30] SLNs [38, 39] Brain [43, 44] Whole body [28, 47]

<sup>a</sup>Optical dependent, determined by NA (numerical aperture) of optical lens and optical wavelength

<sup>b</sup>Acoustic dependent, determined by NA of acoustic lens and acoustic central frequency

<sup>c</sup>Acoustic dependent, determined by acoustic central frequency

<sup>d</sup>Acoustic dependent, determined by acoustic frequency bandwidth

<sup>e</sup>Optical ballistic regime

<sup>f</sup>Optical diffusive regime

<sup>g</sup>SLN: Sentinel Lymph Node

## 2.2 Acoustic-resolution PA Systems

As light travels deeper into the tissue, tight optical focusing is no longer achievable due to multiple scattering events of photons [23]. Correspondingly, for an acoustic-resolution PA system, weakly “focused” light is usually used to excite a significantly larger volume of the sample than that in an optical-resolution PA system (Figure 1b, 1d). However, as acoustic waves are much less scattered than photons in biological tissue, acoustic focusing is superior to optical focusing beyond a specific imaging depth and will yield a lateral resolution that is determined by the ultrasound focusing [4]. The lateral resolution of acoustic-resolution PA systems is typically within hundreds of microns to tens of microns (Table 1), which is scalable with the centre frequency of the ultrasound transducer. Benefitting from the large imaging depth, the acoustic-resolution PA system is more commonly used in whole-body imaging applications (Table 1). Wang *et al.* applied AR-PAM system in conjunction with a novel targeted indocyanine green-doped nanoprobe to image breast cancer in mice (Figure 5) [26]. For AR-PACT systems, three types of detection geometries have been reported: planar [27], circular [28] and spherical [29, 30]. Wang *et al.* presented a three-dimensional volumetric PA imaging system built on a two-dimensional planar matrix array ultrasound probe and demonstrated the clinical potential of the system to identify sentinel lymph nodes for cancer staging purposes (Figure 6) [27]. To perform whole-body imaging, Xia *et al.* reported a novel small animal whole-body PA imaging system with a confocal design of free-space ring-shaped light illumination and 512-element full-ring ultrasonic array signal detection (Figure 7) [28]. Kruger *et al.*

developed a dedicated human breast PA mammography system with a spherical detector capable of spiral scanning (Figure 8) [29, 30]. As mentioned in the optical-resolution systems, the imaging speed of AR-PACT is much higher than that of AR-PAM because no mechanical raster scanning is needed (Table 2).

**Table 2.** Properties of selected AFPs and CPs used in PA imaging.

Protein	Abs <sup>a</sup>	$\epsilon$ at peak <sup>b</sup>	$\epsilon$ at 650 nm <sup>c</sup>	$\Phi^{\text{d}}$	Ref. <sup>e</sup>
EGFP	488	53	0.2	0.6	[69]
DsRed	558	52	1.2	0.68	[70]
E2-Crimson NF <sup>l, g</sup>	583	ND <sup>h</sup>	ND <sup>h</sup>	ND <sup>h</sup>	[67]
mCherry	587	72	0.1	0.22	[71]
Ultramarine <sup>i</sup>	587	64	2.3	0.001	[72]
dUltramarine2 <sup>g</sup>	587	82	~3	<0.0001	[73]
tdUltramarine2 <sup>l, g</sup>	587	203	~7.3	<0.0001	[73]
mKate	588	45	0.2	0.33	[74]
AQ143 <sup>k</sup>	595	90	9.7	0.04	[62]
aeCP597 <sup>l</sup>	597	110	12	ND <sup>h</sup>	[62]
mRaspberry	598	86	1.9	0.15	[75]
mNeptune	600	67	2.2	0.2	[76]
E2-Crimson	605	59	4.6	0.12	[77]
cjBlue <sup>i</sup>	610	67	3.6	<0.0001	[78]
cjBlue2 <sup>g</sup>	603	57	<3.1	<0.0001	[73]
TagRFP657	611	34	4.6	0.1	[79]

<sup>a</sup>Absorbance maximum in nm

<sup>b</sup>Extinction coefficient at peak in units of  $\text{mM}^{-1}\text{cm}^{-1}$  determined by alkali denaturation

<sup>c</sup>Extinction coefficient at 650 nm in units of  $\text{mM}^{-1}\text{cm}^{-1}$  calculated as a product of  $\epsilon$  at peak and excitation or absorption efficiency at 650 nm. Excitation or absorption efficiency is defined as the ratio of excitation or absorption at a given wavelength to that at peak.

<sup>d</sup>Fluorescence quantum yield

<sup>e</sup>Source of data

<sup>f</sup>E2-Crimson's non-fluorescent variant

<sup>g</sup>Naturally occurring chromoproteins

<sup>h</sup>Not determined

<sup>i</sup>Engineered chromoproteins

<sup>j</sup>A tandem fusion of two copies of dUltramarine2

<sup>k</sup>aeCP597's bright variant

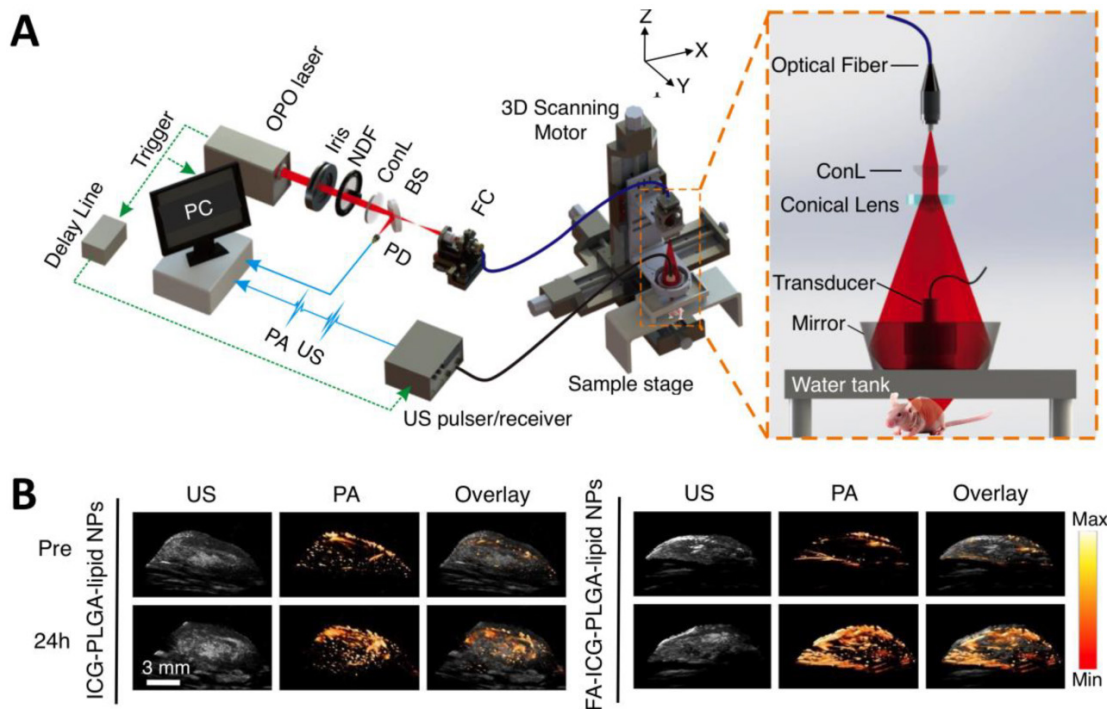


**Figure 5.** AR-PAM imaging of breast cancer *in vivo*. (A) Schematic diagram of the AR-PAM system. OPO: optical parametric oscillator; NDF: neutral density filter; BS: beam splitter; PD: photodiode; FC: optical fiber coupler; PA: photoacoustic; US: ultrasound; ConL: convex lens. (B) Three-dimensional ultrasound (US), PA, and their overlay images of the tumor region before and 24 hours after the injection of non-targeted ICG-PLGA-lipid nanoparticles and targeted FA-ICG-PLGA-lipid nanoparticles, respectively. Figure adapted with permission from [26].

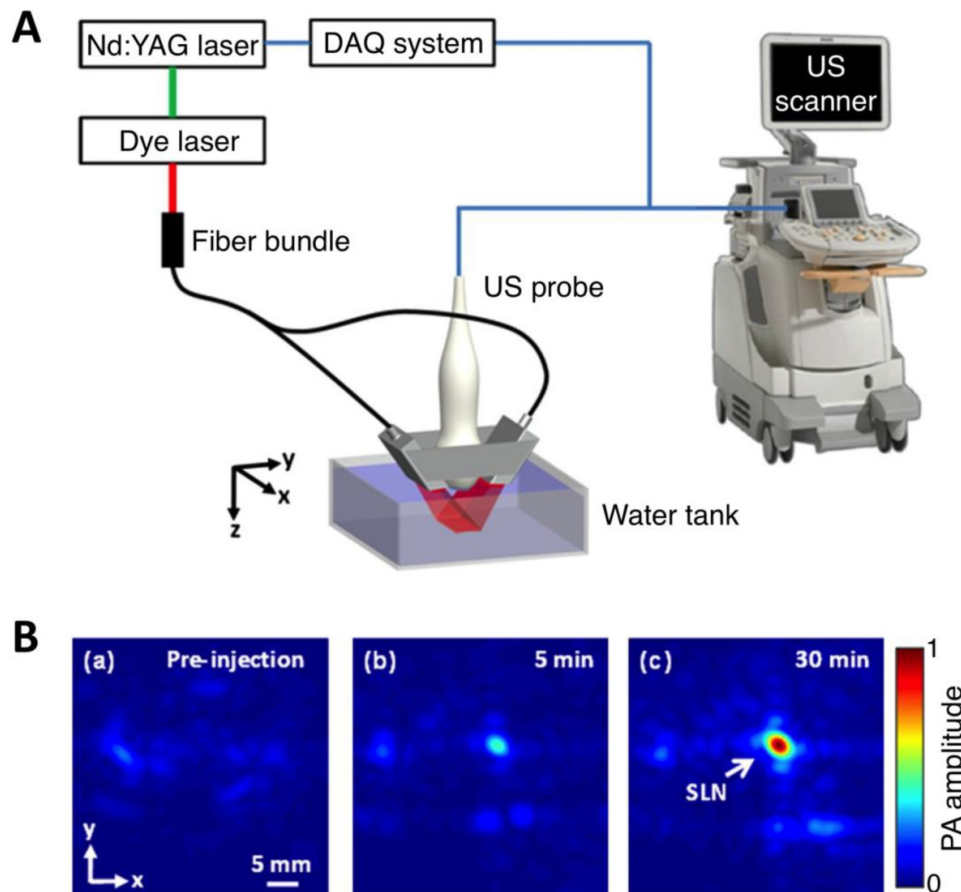


**Figure 6.** Three-dimensional volumetric AR-PACT imaging of sentinel lymph node *in vivo*. (A) Schematic diagram of a volumetric PA imaging system with a matrix probe. DAQ: data acquisition; US: ultrasound. (B) PA images of the rat axillary region obtained (a) before methylene blue dye injection and (b) 5 min and (c) 30 min post injection, indicating the uptake of dye in the sentinel lymph node (SLN). Figure adapted with permission from [27].

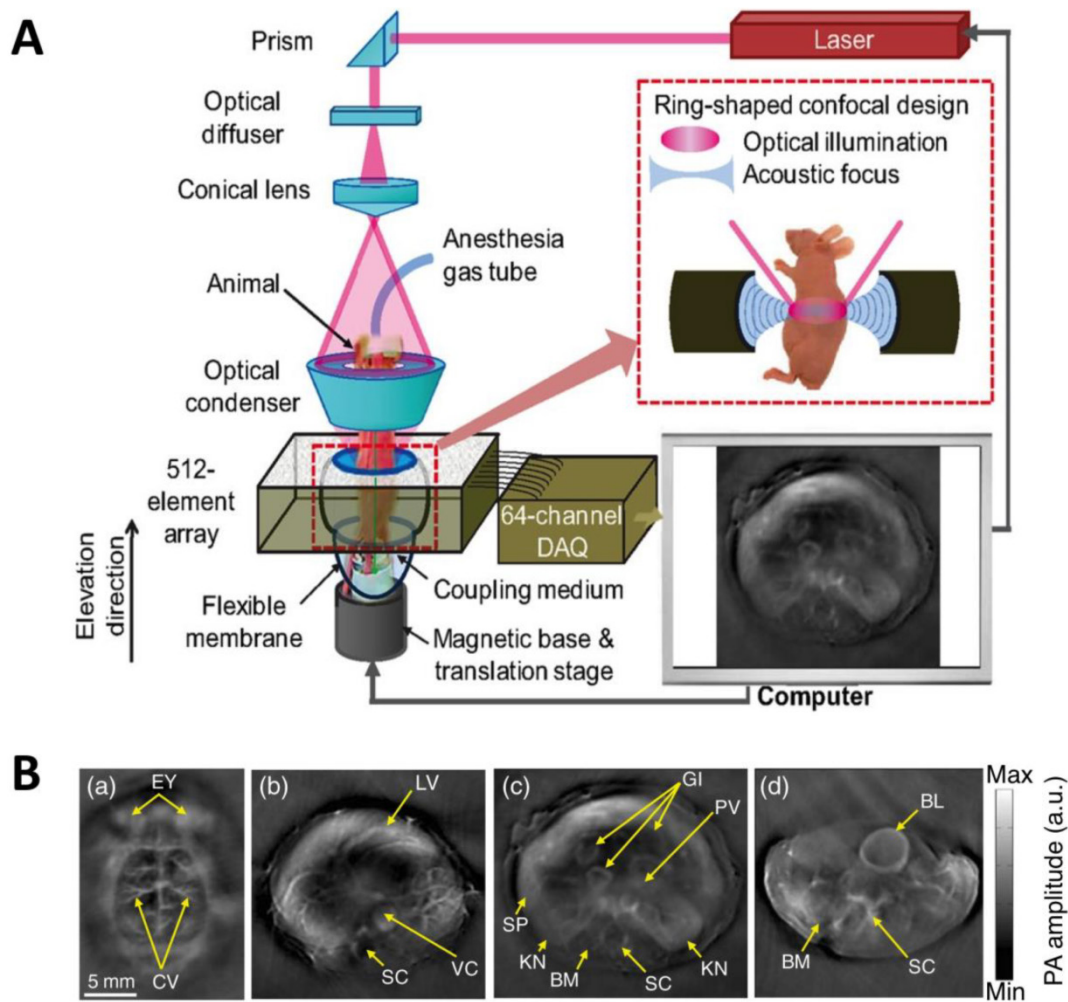


**Figure 7.** Whole-body AR-PACT imaging of a mouse. (A) Schematic diagram of the whole-body PA imaging system. (B) *In vivo* PA images of a mouse acquired noninvasively at various anatomical locations: brain (a); liver (b); kidney (c); and bladder (d). BL, bladder; BM, backbone muscle; CV, cortical vessels; EY, eyes; GI, gastrointestinal tract; KN, kidney; LV, liver; PV, portal vein; SC, spinal cord; SP, spleen; VC, vena cava. Figure adapted with permission from [28].

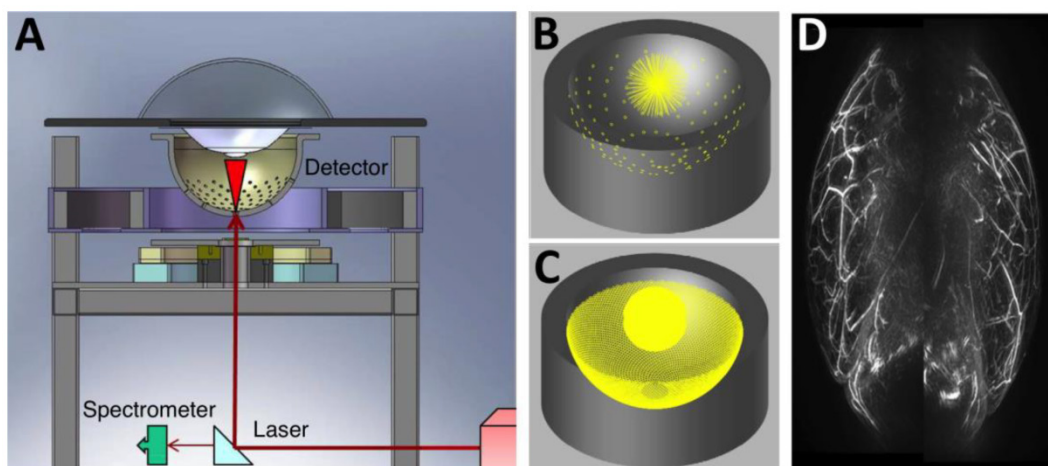


**Figure 8.** Three-dimensional AR-PACT imaging of human breast. (A) Schematic diagram of a human breast PA mammography system, showing the laser beam entering the bottom of the detector bowl and illuminating the sample immersed in water and suspended above the bowl by a transparent tray. A beam splitter allows a portion of the laser beam to be monitored by a spectrometer for detection of laser power and wavelength. (B) The 128 radial projections captured by the detector geometry when data is collected for a single-bowl angular position. (C) The increased density of projections available as the bowl is rotated through 360 degrees. (D) Human breast PA maximum intensity projection image of a healthy volunteer (back-to-back image: left breast on right, right breast on left). Figure adapted with permission from [29, 30].

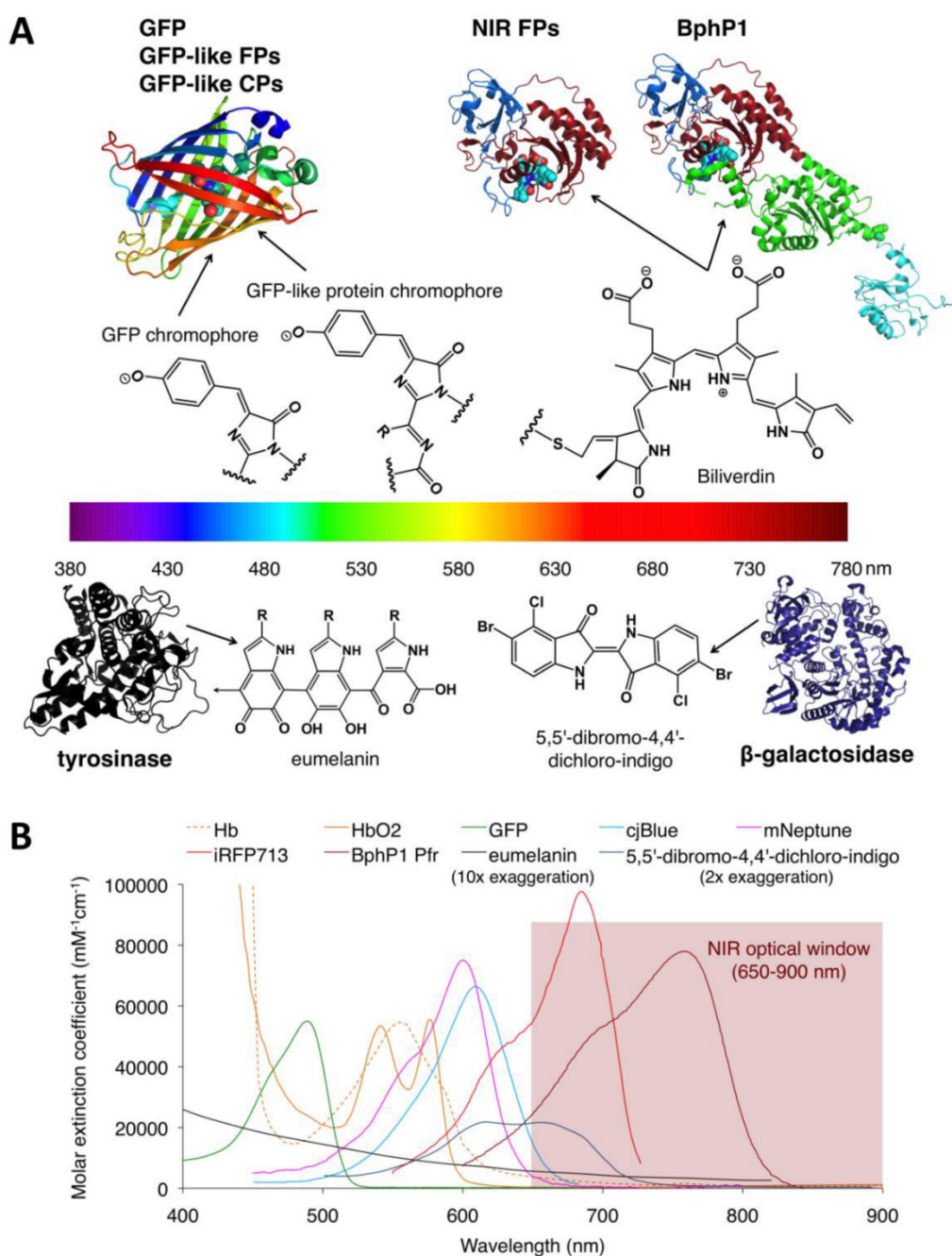


**Figure 9.** Structures and absorbance spectra of genetically encoded PA probes. (A) Diversity of genetically encoded PA probes with distinct chromophores/pigments. The upper and lower parts of the spectrum color bar show the crystal structures of PA probes and the chemical structures of corresponding chromophores or pigments. The chromophores of the probes in the upper part are shown as spheres. In the BphP-based probes (NIR-FPs and BphP1), the PAS domain is shown in blue, the GAF domain in dark red, the PHY domain in green and the output transducing module (OTM) in cyan. Eumelanin is a polymer comprising numerous cross-linked 5,6-dihydroxyindole (DHI) and 5,6-dihydroxyindole-2-carboxylic acid (DHICA). The arrow in eumelanin denotes where the polymer continues. (B) Absorbance spectra of deoxygenated hemoglobin (Hb), oxygenated hemoglobin (HbO<sub>2</sub>), GFP, cjBlue (GFP-like CP), mNeptune (GFP-like FP), iRFP713 (NIR FP), BphP1 Pfr (BphP1 in Pfr state), eumelanin and 5,5'-dibromo-4,4'-dichloro-indigo. Eumelanin and 5,5'-dibromo-4,4'-dichloro-indigo were artificially augmented 10-fold and 2-fold, respectively, to render them visible in the figure. The spectra data for Hb, HbO<sub>2</sub> and eumelanin are from <http://omlc.ogi.edu>, GFP from <http://www.tsienlab.ucsd.edu/Documents.htm>, cjBlue and iRFP713 and 5,5'-dibromo-4,4'-dichloro-indigo from [62], [63] and [53], respectively.

### 3. Genetically Encoded Probes for PA Imaging

#### 3.1 Pigment-producing Enzymes

The metabolic enzymes  $\beta$ -galactosidase (encoded by lacZ) and tyrosinase can produce the

light-absorbing pigments with broad absorption, 5,5'-dibromo-4,4'-dichloro-indigo (blue) and eumelanin (dark brown or black), respectively (Figure 9). Despite a low peak extinction coefficient (EC <10 mM<sup>-1</sup>cm<sup>-1</sup>), naturally occurring pigmented cells, such as melanoma cells, exhibited relatively strong PA signal because the intrinsic signal amplification of

these enzymes produce very high concentrations of pigments in living cells [50, 51]. Mammalian cells that do not naturally contain pigments become light absorber by introducing either  $\beta$ -galactosidase or tyrosinase alone and can be visualized in the presence of substrates using PA imaging [52, 53]. The Wang Lab first established lacZ gene-expressing gliosarcoma tumor cells, imaged lacZ gene expression in tumor at a depth of up to 5 cm with  $\sim$ 1-mm lateral spatial resolution, and obtained well-separated PA images of lacZ and blood vessels [53-55], indicating the utility of  $\beta$ -galactosidase as a PA probe in non-pigmented mammalian cells. However, imaging lacZ expression requires the injection of exogenous X-gal, potentially complicating delivery and metabolism *in vivo* [53]. Moreover, X-gal can cause skin irritation occasionally [53].

In contrast to  $\beta$ -galactosidase, tyrosinase, first found in melanocytes [56], utilizes endogenous and ubiquitous tyrosine in cells as a substrate to produce eumelanin. Thus, tyrosinase is more suited for *in vivo* PA imaging. Transfected cells with human tyrosinase appear darkly pigmented and can be spectrally resolved from hemoglobin *in vivo* using the OR-PAM system [52]. However, with the PACT system, *in vivo* image contrast has been modest [12, 57, 58]. To improve contrast, Jathoul *et al.* developed a new

deep-tissue PA imaging system with a Fabry-Pérot-based optical ultrasound detector, and demonstrated three-dimensional images of tumors at depths up to 8 mm and obtained with a spatial resolution of  $\sim$ 100  $\mu$ m (Figure 10) [13]. Moreover, longitudinal visualization of the growth of human tyrosinase-expressing cells over long periods ( $>$ 7 weeks) *in vivo* has been successfully achieved [13], providing a powerful tool for tracking cell fates over a long time period *in vivo*. Unfortunately, human tyrosinase does not function in bacterial, presumably owing to the difference in the cell membrane of mammalian cells and bacteria. *melA*, a bacterial tyrosinase homologue, has recently been reported as a suitable PA reporter gene for imaging *E. coli* [59], thus providing a complementary method to visualize the infection processes of pathogenic bacteria and monitor bacteria-based cancer treatment *in vivo*. It has been reported that high expression of tyrosinase in mammalian cells is correlated with cytotoxicity as transfected cells do not form melanosome where the cytotoxic semiquinone intermediates generated during eumelanin synthesis are sequestered in melanocytes [60, 61]. Therefore, to minimize the cytotoxicity, the expression level of tyrosinase should be critically controlled in cells [51].

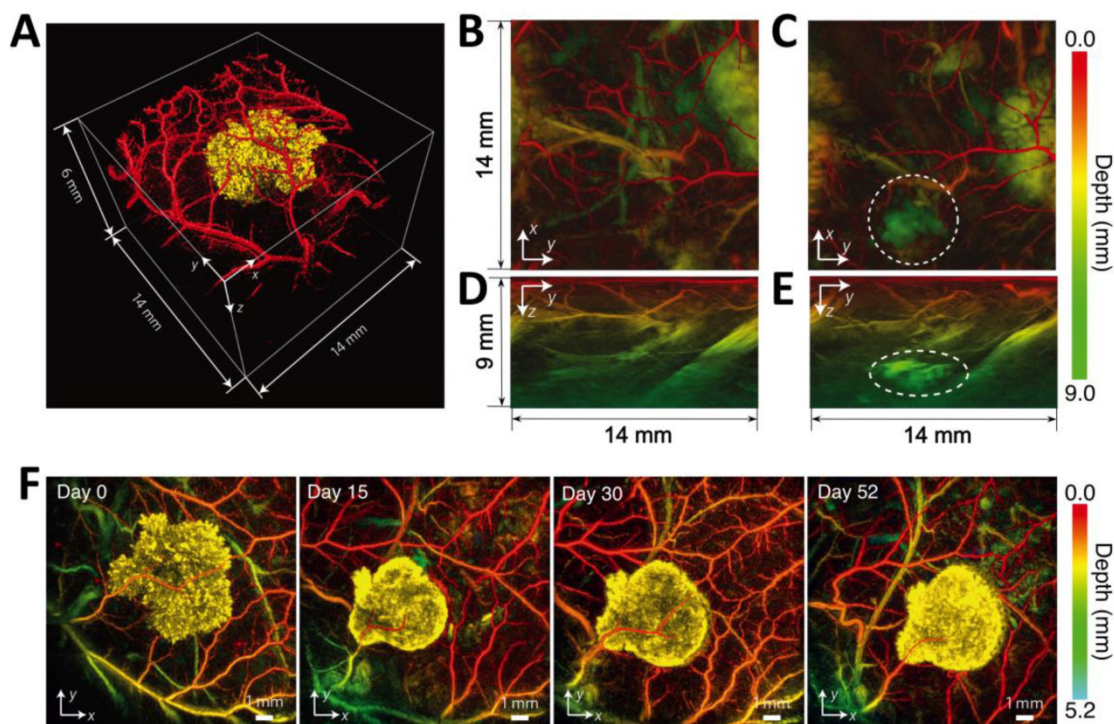


**Figure 10.** *In vivo* PA imaging of tyrosinase-expressing tumor cells after subcutaneous injection into a nude mouse. (A) Volume-rendered image at day 0 post injection. (B-E) Horizontal (x-y, B and C) and vertical (y-z, D and E) maximum amplitude projection (MAP) images of the tumor cell injection area before (B or D) and after (C or E) cell injection. The dotted circles in (C) and (E) indicate the location of the injection. (F) Serial longitudinal *in vivo* MAP images acquired in the same mouse at different time points post inoculation (from 0 to 52 days). Figure adapted with permission from [13].

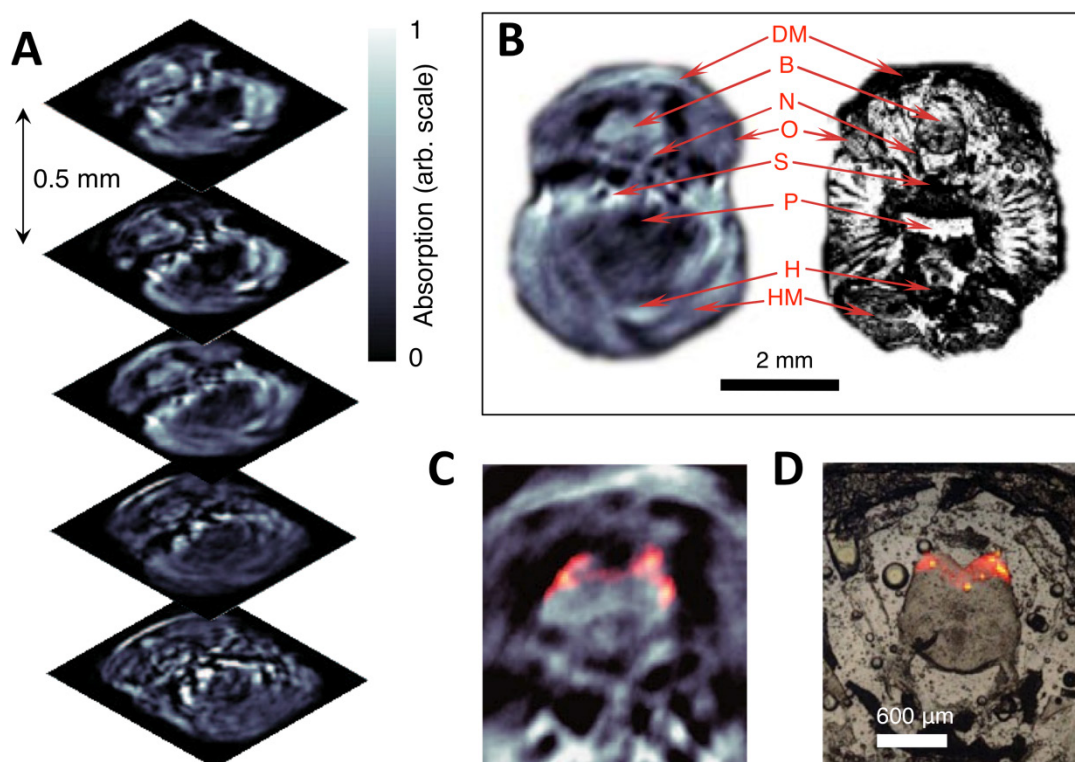


**Figure 11.** Three-dimensional *in vivo* imaging through the brain of an adult mCherry-expressing transgenic zebrafish. (A) Five transverse PA imaging slices through the hindbrain area of a living zebrafish. (B) Example of an imaged slice (left) and its corresponding histological section (right); DM, dorsal fin musculature; B, hindbrain; N, lateral line nerve; O, operculum; S, skull bones; P, pharynx; H, heart; HM, hypobranchial musculature. (C) Multispectral PA tomography image of the brain with mCherry expression shown in color; (D) Corresponding fluorescent histology of a dissected fish at the hindbrain level. Figure adapted with permission from [66].

### 3.2 Fluorescent Proteins and Chromoproteins

#### 3.2.1 Autofluorescent GFP and GFP-like Proteins

Autofluorescent proteins (AFPs) were first isolated from the jellyfish *Aequorea Victoria* (green fluorescent protein, GFP) and subsequently from other marine organisms (GFP-like FPs) [64]. Interestingly, all AFPs share a common structure consisting of an eleven-stranded  $\beta$ -barrel containing an autocatalytically formed chromophore (Figure 9A). AFPs have been widely used as fluorescent markers to monitor protein dynamics in living cells or organisms because they do not require any cofactors or substrates to fluoresce and are non-toxic to mammalian cells [65]. However, AFPs were first used in PA imaging only a few years ago. In 2009, Razansky *et al.* first demonstrated that tissue-specific expression of bright AFPs (GFP and mCherry) several millimeters deep within tissues can be detected using multispectral opto-acoustic tomography (MSOT) with higher spatial resolution than fluorescence (38  $\mu\text{m}$  vs. 1 mm) (Figure 11) [66]. However, due to relatively the high QYs ( $>0.2$ , Table 2) of GFP and mCherry and low absorption in the NIR region (EC at 650 nm  $\leq 0.2$ , Table 2), bright AFP-based PA imaging was limited to relatively transparent zebrafish and small fruit fly pupae [66]. Compared to GFP and red FPs, far-red FPs

have red-shifted absorption spectra and lower QYs, and thus could offer stronger PA signals *in vivo* [67, 68]. However, far-red FPs still exhibit low PA signals due to fluorescence emission and ground-state depopulation effects [67, 68]. Moreover, most far-red FPs can be easily photobleached when exposed to ns excitation pulses typically used in PA imaging [67]. Therefore, photostable and non-fluorescent proteins with strong absorption are required.

#### 3.2.2 Non-fluorescent GFP-like Chromoproteins

Among GFP-like proteins, some non-fluorescent proteins, called chromoproteins (CPs), absorb orange-red light with high ECs ( $>55 \text{ mM}^{-1}\text{cm}^{-1}$ ) and almost negligible QY ( $\leq 0.001$ , Table 2) and are thus better suited as PA probes for *in vivo* PA imaging than far-red FPs. Not surprisingly, compared to far-red FPs with low QYs, two naturally occurring CPs (aeCP597 and cjBlue) exhibit twofold stronger PA signals *in vitro* due to the lack of radiative relaxation, and are more resistant to repeated laser irradiation [67], presumably because of limited oxygen access to the chromophore caused by protein dimerization [80, 81]. To further improve the performance of CPs in PA imaging, several improved cjBlue and Ultramarine variants with 2- to 4-fold increases in PA signals and enhanced photostability were developed using a custom PA screening system [73]. Using a strategy

similar to that employed in engineering fluorescence resonance energy transfer (FRET) biosensors, researchers developed CP-based PA sensors for caspase-3 and successfully visualized caspase-3 activity during staurosporine-induced cell apoptosis in cultured cells [73]. This study was the first to report use of genetically encoded PA biosensors in PA imaging of molecular functions. However, despite these promising results, the low absorption (EC at 650 nm  $\leq 12 \text{ mM}^{-1}\text{cm}^{-1}$ , Table 2) of CPs in the NIR optical window, where the absorption and scattering of light by tissues are minimal, limits their application in highly light-scattering organisms, such as small animals.

### 3.2.3 Bacteriophytochrome-based NIR FPs

Bacteriophytochromes (BphPs) are bacterial photoreceptors that utilize biliverdin IX $\alpha$  (BV) available in mammalian cells as a chromophore [82]. A typical BphP consists of a photosensory core module (PCM) possessing PAS, GAF and PHY domains and an output transducing domain (OTD) (Figure 12A). NIR BphPs, a large subset of BphPs, can convert from the far red-absorbing (Pfr, BV in *trans* form) state to the red-absorbing (Pr, BV in *cis* form) state upon  $\sim 750\text{-nm}$  illumination, and back upon  $\sim 690\text{-nm}$  illumination and *vice versa* (Figure 12B, C). NIR FPs can be achieved by truncating the PHY and effector domains of BphPs and by subsequently introducing specific mutations surrounding BV (Figure 12A and Figure 9A). In contrast to bright AFPs, most BphP-based NIR FPs have low quantum yields ( $<0.10$ ) and high ECs ( $>90 \text{ mM}^{-1}\text{cm}^{-1}$ ) in the NIR optical window (Table 3), and are thus expected to be superior to their visible counterparts. In 2012, Filonov *et al.* first reported that NIR FP iRFP713 exhibits 2-fold higher PA signals than lysed oxygenated blood and far-red FPs under 680-nm excitation and imaged subcutaneous tumors overlaid by 4-mm-thick tissue at a 280- $\mu\text{m}$  lateral resolution with the deep-tissue PAM imaging (Figure 13A) [1], suggesting that NIR FPs are promising probes for deep-tissue PA imaging. Imaging multiple biological events enables several cell populations to be tracked or the interactions between cells and their microenvironment to be monitored. Two new NIR FPs, iRFP670 and iRFP720, were recently developed, and two tumors labeled with iRFP670 and iRFP720 in the presence of blood vessels were simultaneously visualized with submillimeter resolution at a depth of up to 8 mm (Figure 13B) [83]. Up to now, more than fifteen BphP-based NIR FPs with desired properties have been developed (Table 3) and can be extended to functional applications. For example, monomeric mIFP [84] might be used as a protein tag to monitor

gene expression of proteins of interest *in vivo* using PA imaging.

**Table 3.** Properties of BphP-based NIR FPs.

NIR FP	Ex <sup>a</sup>	Em <sup>b</sup>	$\epsilon$ at peak <sup>c</sup>	$\Phi^d$	BphP	Ref. <sup>e</sup>
IFP1.4	684	708	92	0.077	<i>Dr</i> BphP	[86]
Wi-Phy	701	719	93	0.047	<i>Dr</i> BphP	[87]
IFP1.4rev	685	708	131	0.087	<i>Dr</i> BphP	[88]
IFP2.0	690	711	98	0.081	<i>Dr</i> BphP	[89]
iRFP713	690	713	98	0.063	<i>Rp</i> BphP2	[63]
iRFP720	702	720	96	0.06	<i>Rp</i> BphP2	[90]
iRFP713/V256C <sup>f</sup>	662	680	94	0.145	<i>Rp</i> BphP2	[91]
iRFP682	663	682	90	0.113	<i>Rp</i> BphP6	[90]
iRFP702	673	702	93	0.082	<i>Rp</i> BphP6	[90]
iRFP670 <sup>f</sup>	643	670	114	0.111	<i>Rp</i> BphP6	[90]
mIFP	683	704	82	0.084	<i>Br</i> BphP	[84]
iBlueberry <sup>f</sup>	644	667	80	0.08	<i>Br</i> BphP	[92]
GAF-FP <sup>g</sup>	635	670	50	0.073	<i>Rp</i> BphP1	[93]
BphP1-FP/C20S <sup>f</sup>	639	670	82	0.139	<i>Rp</i> BphP1	[94]
AphB variants	$\sim 695$	$\sim 720$	$\sim 80$	$\sim 0.06$	AphB	[95]

<sup>a</sup>Excitation maximum in nm

<sup>b</sup>Emission maximum in nm

<sup>c</sup>Extinction coefficient at peak in units of  $\text{mM}^{-1}\text{cm}^{-1}$  calculated based on BV absorbance

<sup>d</sup>Fluorescence quantum yield

<sup>e</sup>Source of data

<sup>f</sup>BV covalently binds to Cys256 in the GAF domain (the numbering is based on iRFP713)

<sup>g</sup>GAF domain only

Like other imaging modalities, the contrast of PA imaging *in vivo* is determined not only by probe performance but also by tissue background [85]. In PA imaging, the background mainly originates from the tissue absorber hemoglobin in blood through visible and NIR regions. Thus, even with high PA generation efficiency and strong absorption in the NIR region, BphP-based NIR FPs offer relatively low PA contrast over blood *in vivo* ( $\sim 2$ ), limiting visualization of a small number of probes or cells expressing probes in the vasculature. One way to suppress the background is using the difference of PA images corresponding to different locations with specially designed magnetic nanoparticles [85], which suggests that any absorption change in a given imaging area can significantly increase PA contrast. Therefore, a genetically encoded PA probe with optical absorption change should be able to dramatically enhance the imaging contrast *in vivo*.

### 3.3 Reversibly Photoswitchable Proteins

Reversibly photoswitchable proteins (rPSPs) can switch back and forth between two states with well-separated absorption peaks [96], making them useful for high-contrast PA imaging. In rPSP-based PA imaging, PA signals from a rPSP in two light-absorbing states under the illumination of same wavelength light are first recorded, and then pixel-wise subtraction of the images in low

light-absorbing state from the images in high contrast. The conversion of the light-absorbing state is performed to generate a differential image. Up to now, two classes of rPSPs

have been exploited to achieve high-contrast PA images [43, 97].

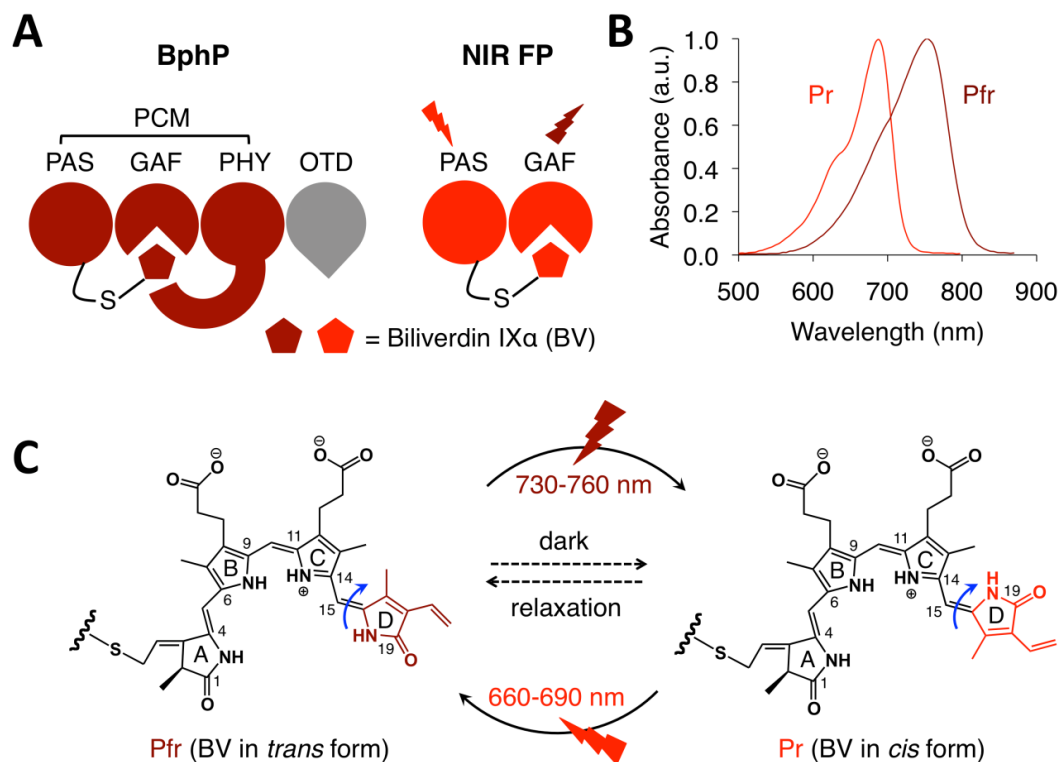


**Figure 12.** Structure and optical properties of bacteriophytochromes (BphPs). (A) Domain organization of BphP. In BphP, BV is secured in the chromophore-binding pocket of the GAF domain and binds covalently to the conserved cysteine residue in the N-terminus of the PAS domain. The chromophore binding module (PAS and GAF domains) can easily be engineered into NIR FPs. PCM: photosensory core module. OTD: output transducing domain. (B) Absorbance spectra of a typical NIR BphP. (C) Conversion between the Pfr state and the Pr state and vice versa is induced by far-red or red light, respectively, owing to *trans-cis* photoisomerization of the D-ring of the BV chromophore around the C15=C16 double bond (blue arrows). In the dark, the photoconverted state spontaneously reverts back to the ground state (dashed arrows).

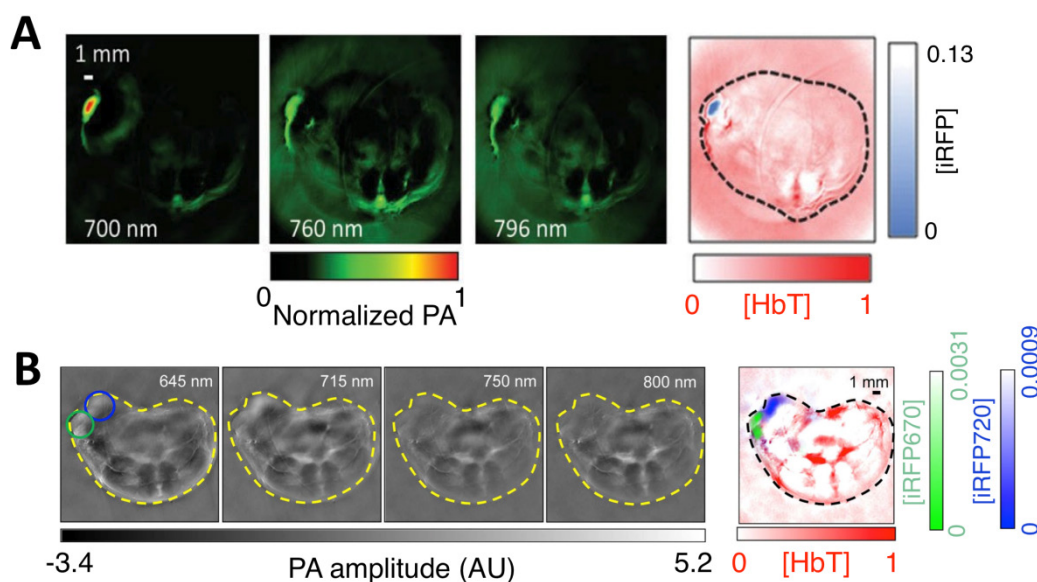


**Figure 13.** *In vivo* PA imaging of tumors expressing iRFP. (A) PA images of mammary gland tumor expressing iRFP713. The three images on the left were acquired at different wavelengths as indicated in the figure; the right-most image is a spectrally separated image with the iRFP713 signal in blue and the blood signal in red. (B) PA images of two different tumors labeled with iRFP670 and iRFP720. The four images on the left were acquired at different wavelengths as indicated in the figure; the right-most image is the spectrally separated image with the iRFP670 signal in blue, the iRFP720 signal in green, and the blood signal in red. Figure adapted with permission from [83].

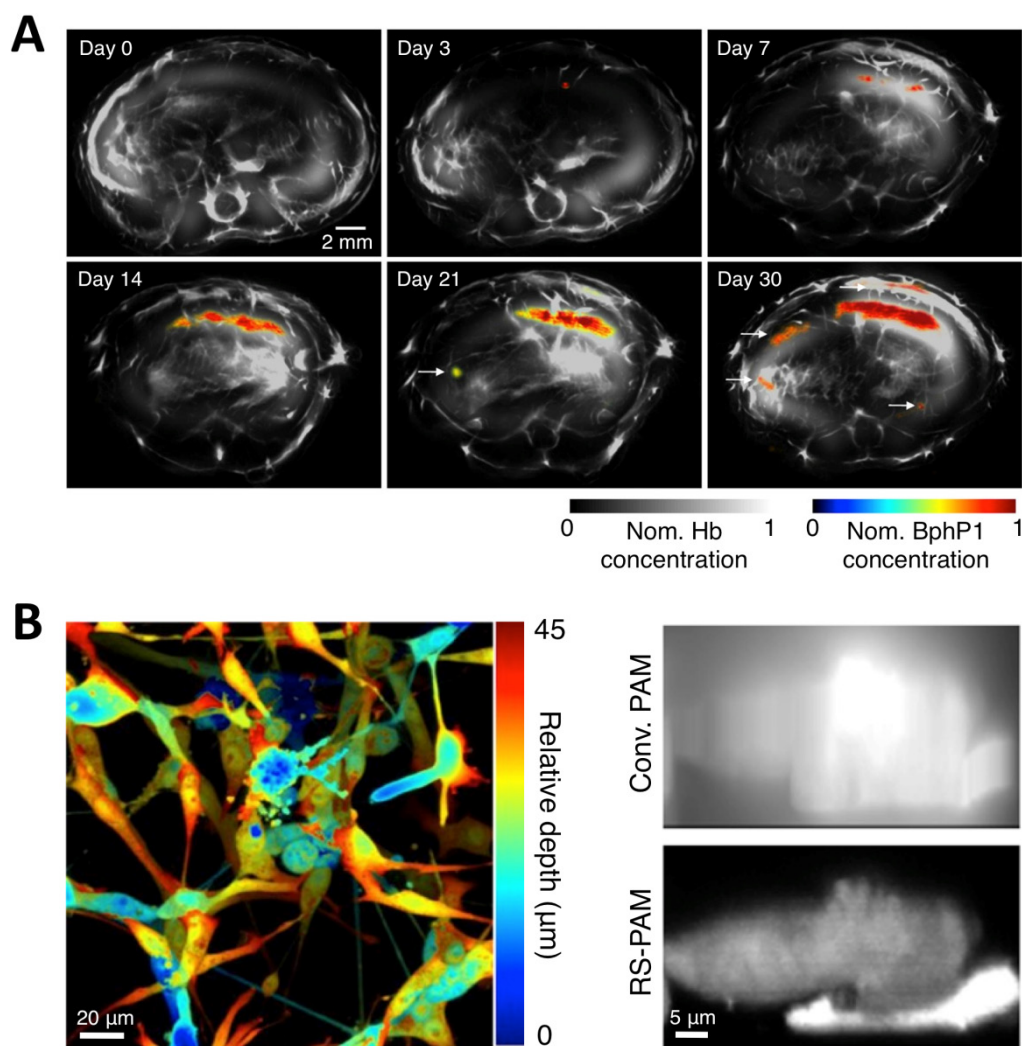


**Figure 14.** Multiscale PA imaging of photoswitchable BphP1 with high contrast and resolution. (A) *In vivo* longitudinal PA monitoring of cancer metastasis in mouse liver for 30 days after the injection of tumor cells expressing BphP1 into the right liver lobe. Differential signals (in color) are overlaid on top of the structure signals from blood (in gray scale). The white arrows in the images for day 21 and 30 indicate secondary tumors due to metastasis. (B) Super-resolution RS-PAM imaging of U87 cells expressing BphP1. Left: depth-encoded RS-PAM image of a multilayered BphP1-expressing fixed U87 cells; Right: x-z cross-sectional images of two stacked U87 cells expressing BphP1, acquired with conventional PAM (Conv. PAM) and RS-PAM, demonstrating the substantially finer axial resolution of RS-PAM. Figure adapted with permission from [43].

Two reversibly switchable green FPs, Dronpa and its fast-switching variant Dronpa-M159T (both are GFP-like AFPs) were first applied to PA imaging. By photoswitching the two Dronpa variants with a programmed optical illumination schedule, two FPs can be distinguished from each other and from the strong background signals with an increase in signal-to-noise ratio (SNR) by a factor of 5 using the temporally unmixed MSOT technique. However, as discussed above, Dronpa and Dronpa-M159T have very high fluorescence QY ( $\sim 0.85$ ) and low absorption in the NIR region and thus are not suitable for deep tissue PA imaging.

To overcome the limitations of Dronpa, very recently, Yao *et al.* reported a novel high-contrast imaging approach that combines deep tissue PA imaging with the NIR photochromic protein BphP1, the full-length *Rp*BphP1 bacteriophytochrome from

*Rhodospseudomonas palustris* (Figure 12A) [43]. BphP1 adopts the Pfr state in the dark and can switch off (Pr state) and on (Pfr state) upon 780-nm and 630-nm light illumination (Figure 12B, C), respectively. Surprisingly, the contrast-to-noise ratio (CNR) for the differential image was 21 while that of the Pfr-state image was  $\sim 1$  at a 10-mm depth in the scattering medium, indicating that background reduction with rPSPs can significantly increase the PA imaging contrast. To demonstrate the ability of BphP1 to visualize weak signals deep in tissues, the growth and metastasis of tumor expressing BphP1 in mouse livers were monitored over a long time period (30 days). Lateral resolution of  $\sim 100 \mu\text{m}$  was obtained with an average CNR of  $\sim 15$  (Figure 14A). In addition, a sub-diffraction spatial resolution of 140 nm on individual cancer cells was achieved using RS-PAM (reversible photoswitching PAM), a two-fold

improvement over that of traditional PAM (Figure 14B), enabling multiscale PA imaging using the BphP1-based single-wavelength differential method.

The BphP1-based single-wavelength differential-imaging method has several advantages over the conventional method with non-photoswitchable probes. First, BphP1 is the most red-shifted of all reported BphPs, with an absorption peak at 760 nm, thus enabling deep-tissue PA imaging. Second, BphP1 resists photobleaching during photoconversion and imaging, enabling longitudinal imaging. Third, BphP1 photoconverts much more easily *in vivo* than photoswitchable AFPs, such as rsTagRFP because red and NIR light attenuate much less than blue and orange light do *in vivo*. In addition, even under daylight, a portion of BphP1 can undergo the Pr-Pfr transition. Fourth, the formation of the chromophore BV in BphP1 is oxygen independent, whereas GFP-like proteins require oxygen. Thus, BphP1 is more suitable for hypoxic tissues. Finally, compared to conventional multispectral methods, single-wavelength imaging at 780 nm greatly reduces the unknown influence of local light fluence. Therefore, the single-wavelength differential-imaging method combined with the photoswitchable BphP1 is the most promising approach for detection of weak signals from molecules and cells deep in living subjects.

#### 4. Concluding Remarks and Outlook

Over the past two decades, different PA imaging technologies have been rapidly developed to circumvent the limited penetration depth and spatial resolution of conventional optical imaging *in vivo*. Deep-tissue PA imaging using genetically encoded reporter genes, particularly photoswitchable BphP1, offers a powerful tool for tracking cell fates and molecular functions in deep tissue within light-scattering living organisms. Although, unlike chemical dyes or nanoparticles, the use of BphP1 in humans remains challenging due to the requirement of introduction of exogenous genetic material [20] and potential safety issues [98], PA imaging with BphP1 provides unprecedented detection sensitivity and penetration depth and is thus useful for both basic research such as cancer, developmental biology and neurosciences and preclinical applications in small animals [10, 99, 100].

Currently, PA imaging has found broad applications both in preclinical laboratory research and clinical studies and trials. However, more work is needed to further mature this imaging technology and accelerate its clinical translation. 1) To fully explore the multi-scale capability of PA imaging, a novel system design that can achieve multiple optical

resolutions by easily switching optical objectives, achieve multiple acoustic resolutions by easily switching ultrasonic transducers, and, finally, achieve full-scale PA imaging by integrating optical- and acoustic-resolution capabilities within a single PA system should be proposed. 2) Accurate quantitative PA imaging methodologies must be developed by considering both the optical and acoustic heterogeneities of biological tissues and by establishing a more sophisticated spectral unmixing model. 3) Multimodality imaging integrating PA with other imaging techniques such as ultrasound or fluorescence imaging should be further developed to provide complementary information on tissue properties *in vivo* [101]. 4) PA systems with new imaging setups and more advanced lasers should be built to further improve imaging speed. For example, the current PACT system for BphP1 has relatively low temporal resolution: 11 min for 20 averaging switching cycles. However, many biological processes in living cells occur on a timescale of nanoseconds to seconds [102]. The imaging speed can be improved using a laser with a higher repetition rate and a 512-channel data-acquisition system, to avoid data multiplexing and thus reduce the imaging time [43]. 5) With the advances in laser technologies, and continuous enhancements of the performance of PA imaging systems, more clinical trials and studies are expected to fully demonstrate the potential of this technology.

Because BphP-based single-wavelength differential PA imaging offers the best performance among all genetically encoded PA probes, future studies should focus on its performance enhancement and development of BphP1-based PA biosensors. 1) Detection sensitivity can be improved by employing superior BphPs with low unconverted efficiency (uCE) and strong absorption in cells. As a differential imaging method, detection is based on the difference between the Pr state and Pfr state, and theoretically, the detection sensitivity is inversely proportional to uCE. The uCE of BphP1 is relatively high, reaching ~20% [43]. In addition, BphP1-expressing cells have relatively weak absorption presumably due to the short lifetime or low BV-binding affinity in cells, or poor maturation and folding of BphP1 or a low EC. New BphPs with strong absorption and low uCE values may be obtained by directed protein evolution of BphP1 or by seeking better ones in nature. 2) Development of BphP1-based PA biosensors. Very few PA studies have sought to visualize molecular function *in vivo* due to the lack of biosensors for PA imaging [73, 103, 104]. By contrast, numerous FP-based fluorescent biosensors are available and can be classified into three major groups with different

design strategies: two FP-based FRET [105], and single FP-based circular permutation [105] and fluorescence complementation [106]. BphP-based NIR FPs have recently been engineered as biosensors to sense protease activity (FRET and circular permutation) [107, 108] and protein-protein interactions (fluorescence complementation) *in vivo* [109]. Since NIR FPs are derived from BphPs, researchers may develop BphP1-based PA biosensors by adopting similar strategies and visualize the spatio-temporal dynamics of biological molecules *in vivo*.

Until recently, most applications based on genetically encoded PA probes have been developed as proof-of-concepts. By utilizing BphP-based differential PA imaging combined with biological models, some long-standing biological questions may be addressed. For example, how do neurons connect with each other during development? [110], and how do key proteins in living cells interact with one another under physiological and pathological conditions *in vivo*? [111]. In summary, the potential capabilities of the BphP1-based single-wavelength differential method are only beginning to be recognized and will be fully explored in the future.

## Abbreviations

PA: photoacoustic; NIR: near-infrared; OCT: optical coherence tomography; OR-PAM: optical-resolution photoacoustic microscopy; AR-PAM: acoustic-resolution photoacoustic microscopy, OR-PACT: optical-resolution photoacoustic computed tomography; AR-PACT: acoustic-resolution photoacoustic computed tomography; QY: quantum yield; EC: Extinction coefficient; NA: numerical aperture; Hb: deoxygenated hemoglobin; HbO<sub>2</sub>: oxygenated hemoglobin; GFP: green fluorescent protein; AFP: autofluorescent proteins; FP: fluorescent protein; MSOT: multispectral opto-acoustic tomography; CP: chromoprotein; FRET: fluorescence resonance energy transfer; BphP: bacteriophytochrome; BV: biliverdin IX<sub>α</sub>; PCM: photosensory core module; OTD: output transducing domain; rPSP: reversibly photoswitchable protein; SNR: signal-to-noise ratio; CNR: contrast-to-noise ratio; uCE: unconverted efficiency; MAP: maximum projection amplitude; RS-PAM: reversible photoswitching PAM

## Acknowledgements

The authors gratefully acknowledge the following funds: 1. NSFC grants 61405234 and 81430038 and 973 program grant 2015CB755500 to C. L.; 2. Shenzhen Science and Technology Innovation grant JCYJ20150521144320987 and the 'Hundred

Talents' Program Award (Y64401) of the Chinese Academy of Sciences and the National Natural Science Foundation of China grant 1431670872 to J.C.; 3. National Natural Science Foundation of China (NSFC) grants 81522024 and 81427804, National Key Basic Research (973) Program of China grant 2014CB744503, International Science and Technology Cooperation Program of China (MOST) grant 2014DFG32800, and Guangdong Science and Technology grants 2013B091500090 and 2014B050505013 to L. S.; 4. NSFC grant 61475182 and Shenzhen Science and Technology Innovation grant JCYJ20150521144321005 to X. G.; NSFC grant 81471778 to Z. W. We apologize to those whose work could not be cited due to space limitations. Emily Wang (Harvard University) and Dr. Michael Lin (Stanford University) for critical reading of the manuscript, and Dr. Gang Han (University of Massachusetts Medical School) for his kind invitation and encouragement.

## Competing Interests

The authors have declared that no competing interest exists.

## References

- Filonov GS, Krumholz A, Xia J, Yao J, Wang LV, Verkhusha VV. Deep-tissue photoacoustic tomography of a genetically encoded near-infrared fluorescent probe. *Angew Chem Int Ed Engl.* 2012; 51: 1448-51.
- Li C, Wang LV. Photoacoustic tomography and sensing in biomedicine. *Phys Med Biol.* 2009; 54: R59-97.
- Grootendorst DJ, Jose J, Wouters MW, van Boven H, Van der Hage J, Van Leeuwen TG, et al. First experiences of photoacoustic imaging for detection of melanoma metastases in resected human lymph nodes. *Lasers Surg Med.* 2012; 44: 541-9.
- Wang LV, Hu S. Photoacoustic tomography: *in vivo* imaging from organelles to organs. *Science.* 2012; 335: 1458-62.
- Yao J, Song L, Wang LV. Photoacoustic microscopy: superdepth, superresolution, and superb contrast. *IEEE Pulse.* 2015; 6: 34-7.
- Wang LV. Multiscale photoacoustic microscopy and computed tomography. *Nat Photonics.* 2009; 3: 503-9.
- Guo Z, Li L, Wang LV. On the speckle-free nature of photoacoustic tomography. *Med Phys.* 2009; 36: 4084-8.
- Razansky D, Deliolanis NC, Vinegoni C, Ntziachristos V. Deep tissue optical and photoacoustic molecular imaging technologies for pre-clinical research and drug discovery. *Curr Pharm Biotechnol.* 2012; 13: 504-22.
- Liu Y, Nie L, Chen X. Photoacoustic Molecular Imaging: From Multiscale Biomedical Applications Towards Early-Stage Theranostics. *Trends Biotechnol.* 2016; 34: 420-33.
- Yao J, Wang LV. Photoacoustic Brain Imaging: from Microscopic to Macroscopic Scales. *NeuroPhotonics.* 2014; 1.
- Wang LV. Prospects of photoacoustic tomography. *Med Phys.* 2008; 35: 5758-67.
- Stritzker J, Kirscher L, Scadeng M, Deliolanis NC, Morscher S, Symvoulidis P, et al. Vaccinia virus-mediated melanin production allows MR and photoacoustic deep tissue imaging and laser-induced thermotherapy of cancer. *Proc Natl Acad Sci U S A.* 2013; 110: 3316-20.
- Jathoul AP, Laufer J, Ogunlade O, Treeby B, Cox B, Zhang E, et al. Deep *in vivo* photoacoustic imaging of mammalian tissues using a tyrosinase-based genetic reporter. *Nature Photonics.* 2015; 9: 8.
- Dragulescu-Andrasi A, Kothapalli SR, Tikhomirov GA, Rao J, Gambhir SS. Activatable oligomerizable imaging agents for photoacoustic imaging of furin-like activity in living subjects. *J Am Chem Soc.* 2013; 135: 11015-22.
- Yang Q, Cui H, Cai S, Yang X, Forrest ML. *In vivo* photoacoustic imaging of chemotherapy-induced apoptosis in squamous cell carcinoma using a near-infrared caspase-9 probe. *J Biomed Opt.* 2011; 16: 116026.
- Hu S, Maslov K, Wang LV. Second-generation optical-resolution photoacoustic microscopy with improved sensitivity and speed. *Opt Lett.* 2011; 36: 1134-6.

17. Song W, Zheng W, Liu R, Lin R, Huang H, Gong X, et al. Reflection-mode in vivo photoacoustic microscopy with subwavelength lateral resolution. *Biomed Opt Express*. 2014; 5: 4235-41.
18. Weight RM, Dale PS, Viator JA. Detection of circulating melanoma cells in human blood using photoacoustic flowmetry. *Conf Proc IEEE Eng Med Biol Soc*. 2009; 2009: 106-9.
19. Yang X, Stein EW, Ashkenazi S, Wang LV. Nanoparticles for photoacoustic imaging. *Wiley Interdiscip Rev Nanomed Nanobiotechnol*. 2009; 1: 360-8.
20. Zackrisson S, van de Ven SM, Gambhir SS. Light in and sound out: emerging translational strategies for photoacoustic imaging. *Cancer Res*. 2014; 74: 979-1004.
21. Nie L, Chen X. Structural and functional photoacoustic molecular tomography aided by emerging contrast agents. *Chem Soc Rev*. 2014; 43: 7132-70.
22. Longmire M, Choyke PL, Kobayashi H. Clearance properties of nano-sized particles and molecules as imaging agents: considerations and caveats. *Nanomedicine (Lond)*. 2008; 3: 703-17.
23. Wang LV, HU HI. *Biomedical Optics: Principles and Imaging*. Wiley-Interscience; 2007.
24. Chen J, Lin R, Wang H, Meng J, Zheng H, Song L. Blind-deconvolution optical-resolution photoacoustic microscopy in vivo. *Opt Express*. 2013; 21: 7316-27.
25. Song L, Maslov K, Wang LV. Multifocal optical-resolution photoacoustic microscopy in vivo. *Opt Lett*. 2011; 36: 1236-8.
26. Wang H, Liu C, Gong X, Hu D, Lin R, Sheng Z, et al. In vivo photoacoustic molecular imaging of breast carcinoma with folate receptor-targeted indocyanine green nanoprobes. *Nanoscale*. 2014; 6: 14270-9.
27. Wang Y, Erpelding TN, Jankovic L, Guo Z, Robert JL, David G, et al. In vivo three-dimensional photoacoustic imaging based on a clinical matrix array ultrasound probe. *J Biomed Opt*. 2012; 17: 061208.
28. Xia J, Chatni MR, Maslov K, Guo Z, Wang K, Anastasio M, et al. Whole-body ring-shaped confocal photoacoustic computed tomography of small animals in vivo. *J Biomed Opt*. 2012; 17: 050506.
29. Lam RB, Kruger RA, Reinecke DR, DelRio S, Thornton MM, Picot PA, et al. Dynamic optical angiography of mouse anatomy using radial projections. *Proc of SPIE*. 2010; 7564: 7.
30. Kruger RA, Kuzmiak CM, Lam RB, Reinecke DR, Del Rio SP, Steed D. Dedicated 3D photoacoustic breast imaging. *Med Phys*. 2013; 40: 113301.
31. Ning B, Sun N, Cao R, Chen R, Kirk Shung K, Hossack JA, et al. Ultrasound-aided Multi-parametric Photoacoustic Microscopy of the Mouse Brain. *Sci Rep*. 2015; 5: 18775.
32. Yao J, Wang L, Yang JM, Maslov KI, Wong TT, Li L, et al. High-speed label-free functional photoacoustic microscopy of mouse brain in action. *Nat Methods*. 2015; 12: 407-10.
33. Xia J, Li G, Wang L, Nasirivanaki M, Maslov K, Engelbach JA, et al. Wide-field two-dimensional multifocal optical-resolution photoacoustic-computed microscopy. *Opt Lett*. 2013; 38: 5236-9.
34. Kim C, Cho EC, Chen J, Song KH, Au L, Favazza C, et al. In vivo molecular photoacoustic tomography of melanomas targeted by bioconjugated gold nanocages. *ACS Nano*. 2010; 4: 4559-64.
35. Lin R, Chen J, Wang H, Yan M, Zheng W, Song L. Longitudinal label-free optical-resolution photoacoustic microscopy of tumor angiogenesis in vivo. *Quant Imaging Med Surg*. 2015; 5: 23-9.
36. Meng J, Wang LV, Liang D, Song L. In vivo optical-resolution photoacoustic computed tomography with compressed sensing. *Opt Lett*. 2012; 37: 4573-5.
37. Kim C, Song KH, Gao F, Wang LV. Sentinel lymph nodes and lymphatic vessels: noninvasive dual-modality in vivo mapping by using indocyanine green in rats—volumetric spectroscopic photoacoustic imaging and planar fluorescence imaging. *Radiology*. 2010; 255: 442-50.
38. Erpelding TN, Kim C, Pramanik M, Jankovic L, Maslov K, Guo Z, et al. Sentinel lymph nodes in the rat: noninvasive photoacoustic and US imaging with a clinical US system. *Radiology*. 2010; 256: 102-10.
39. Song L, Kim C, Maslov K, Shung KK, Wang LV. High-speed dynamic 3D photoacoustic imaging of sentinel lymph node in a murine model using an ultrasound array. *Med Phys*. 2009; 36: 3724-9.
40. Hu S, Maslov K, Wang LV. Noninvasive label-free imaging of microhemodynamics by optical-resolution photoacoustic microscopy. *Opt Express*. 2009; 17: 7688-93.
41. Nie L, Guo Z, Wang LV. Photoacoustic tomography of monkey brain using virtual point ultrasonic transducers. *J Biomed Opt*. 2011; 16: 076005.
42. Kircher MF, de la Zerda A, Jokerst JV, Zavaleta CL, Kempen PJ, Mittra E, et al. A brain tumor molecular imaging strategy using a new triple-modality MRI-photoacoustic-Raman nanoparticle. *Nat Med*. 2012; 18: 829-34.
43. Yao J, Kaberniuk AA, Li L, Shcherbakova DM, Zhang R, Wang L, et al. Multiscale photoacoustic tomography using reversibly switchable bacterial phytochrome as a near-infrared photochromic probe. *Nat Methods*. 2016; 13: 67-73.
44. Nasirivanaki M, Xia J, Wan H, Bauer AQ, Culver JP, Wang LV. High-resolution photoacoustic tomography of resting-state functional connectivity in the mouse brain. *Proc Natl Acad Sci U S A*. 2014; 111: 21-6.
45. Wang L, Maslov K, Wang LV. Single-cell label-free photoacoustic flowimaging in vivo. *Proc Natl Acad Sci U S A*. 2013; 110: 5759-64.
46. Jeon M, Kim J, Kim C. Multiplane spectroscopic whole-body photoacoustic imaging of small animals in vivo. *Med Biol Eng Comput*. 2016; 54: 283-94.
47. Brecht HP, Su R, Fronheiser M, Ermilov SA, Conjusteau A, Oraevsky AA. Whole-body three-dimensional optoacoustic tomography system for small animals. *J Biomed Opt*. 2009; 14: 064007.
48. Yao J, Maslov KI, Shi Y, Taber LA, Wang LV. In vivo photoacoustic imaging of transverse blood flow by using Doppler broadening of bandwidth. *Opt Lett*. 2010; 35: 1419-21.
49. Zhang C, Maslov K, Wang LV. Subwavelength-resolution label-free photoacoustic microscopy of optical absorption in vivo. *Opt Lett*. 2010; 35: 3195-7.
50. O'Brien CM, Rood KD, Bhattacharyya K, DeSouza T, Sengupta S, Gupta SK, et al. Capture of circulating tumor cells using photoacoustic flowmetry and two phase flow. *J Biomed Opt*. 2012; 17: 061221.
51. Papproski RJ, Forbrich AE, Wachowicz K, Hitt MM, Zemp RJ. Tyrosinase as a dual reporter gene for both photoacoustic and magnetic resonance imaging. *BIOMEDICAL OPTICS EXPRESS*. 2011; 2: 10.
52. Krumholz A, Vanvickel-Chavez SJ, Yao J, Fleming TP, Gillanders WE, Wang LV. Photoacoustic microscopy of tyrosinase reporter gene in vivo. *J Biomed Opt*. 2011; 16: 080503.
53. Li L, Zemp RJ, Lungu G, Stoica C, Wang LV. Photoacoustic imaging of lacZ gene expression in vivo. *J Biomed Opt*. 2007; 12: 020504.
54. Li L, Zhang HF, Zemp RJ, Maslov K, Wang L. Simultaneous imaging of a lacZ-marked tumor and microvasculature morphology in vivo by dual-wavelength photoacoustic microscopy. *J Innov Opt Health Sci*. 2008; 1: 207-15.
55. Cai X, Li L, Krumholz A, Guo Z, Erpelding TN, Zhang C, et al. Multi-scale molecular photoacoustic tomography of gene expression. *PLoS One*. 2012; 7: e43999.
56. del Marmol V, Beermann F. Tyrosinase and related proteins in mammalian pigmentation. *FEBS Lett*. 1996; 381: 165-8.
57. Qin C, Cheng K, Chen K, Hu X, Liu Y, Lan X, et al. Tyrosinase as a multifunctional reporter gene for Photoacoustic/MRI/PET triple modality molecular imaging. *Sci Rep*. 2013; 3: 1490.
58. Papproski RJ, Heinmiller A, Wachowicz K, Zemp RJ. Multi-wavelength photoacoustic imaging of inducible tyrosinase reporter gene expression in xenograft tumors. *Sci Rep*. 2014; 4: 5329.
59. Papproski RJ, Li Y, Barber Q, Lewis JD, Campbell RE, Zemp R. Validating tyrosinase homologue melA as a photoacoustic reporter gene for imaging *Escherichia coli*. *J Biomed Opt*. 2015; 20: 106008.
60. van der Poel S, Wolthoorn J, van den Heuvel D, Egmond M, Groux-Degroote S, Neumann S, et al. Hyperacidification of trans-Golgi network and endo/lysosomes in melanocytes by glucosylceramide-dependent V-ATPase activity. *Traffic*. 2011; 12: 1634-47.
61. Weissleder R, Simonova M, Bogdanova A, Bredow S, Enoch WS, Bogdanov A, Jr. MR imaging and scintigraphy of gene expression through melanin induction. *Radiology*. 1997; 204: 425-9.
62. Shkrob MA, Yanushevich YG, Chudakov DM, Gurskaya NG, Labas YA, Poponov SY, et al. Far-red fluorescent proteins evolved from a blue chromoprotein from *Actinia equina*. *Biochem J*. 2005; 392: 649-54.
63. Filonov GS, Piatkevich KD, Ting LM, Zhang J, Kim K, Verkhusha VV. Bright and stable near-infrared fluorescent protein for in vivo imaging. *Nat Biotechnol*. 2011; 29: 757-61.
64. Drepper T, Eggert T, Circolone F, Heck A, Krauss U, Guterl JK, et al. Reporter proteins for in vivo fluorescence without oxygen. *Nat Biotechnol*. 2007; 25: 443-5.
65. Mishin AS, Belousov VV, Solntsev KM, Lukyanov KA. Novel uses of fluorescent proteins. *Curr Opin Chem Biol*. 2015; 27: 1-9.
66. Razansky D, Distel M, Vinegoni C, Ma R, Perrimon N, Koster RW, et al. Multispectral opto-acoustic tomography of deep-seated fluorescent proteins in vivo. *Nature Photonics*. 2009; 3: 6.
67. Laufer J, Jathoul A, Pule M, Beard P. In vitro characterization of genetically expressed absorbing proteins using photoacoustic spectroscopy. *Biomed Opt Express*. 2013; 4: 2477-90.
68. Deliolanis NC, Ale A, Morscher S, Burton NC, Schaefer K, Radrich K, et al. Deep-tissue reporter-gene imaging with fluorescence and optoacoustic tomography: a performance overview. *Mol Imaging Biol*. 2014; 16: 652-60.
69. Patterson GH, Knobel SM, Sharif WD, Kain SR, Piston DW. Use of the green fluorescent protein and its mutants in quantitative fluorescence microscopy. *Biophys J*. 1997; 73: 2782-90.
70. Bevis BJ, Glick BS. Rapidly maturing variants of the *Drosophila* red fluorescent protein (DsRed). *Nat Biotechnol*. 2002; 20: 83-7.
71. Shaner NC, Campbell RE, Steinbach PA, Giepmans BN, Palmer AE, Tsien RY. Improved monomeric red, orange and yellow fluorescent proteins derived from *Drosophila* sp. red fluorescent protein. *Nat Biotechnol*. 2004; 22: 1567-72.
72. Pettikiriarachchi A, Gong L, Perugini MA, Devenish RJ, Prescott M. Ultramarine, a chromoprotein acceptor for Förster resonance energy transfer. *PLoS One*. 2012; 7: e41028.
73. Li Y, Forbrich A, Wu J, Shao P, Campbell RE, Zemp R. Engineering Dark Chromoprotein Reporters for Photoacoustic Microscopy and FRET Imaging. *Sci Rep*. 2016; 6: 22129.
74. Shcherbo D, Merzlyak EM, Chepurnykh TV, Fradkov AF, Ermakova GV, Solovieva EA, et al. Bright far-red fluorescent protein for whole-body imaging. *Nat Methods*. 2007; 4: 741-6.
75. Wang L, Jackson WC, Steinbach PA, Tsien RY. Evolution of new nonantibody proteins via iterative somatic hypermutation. *Proc Natl Acad Sci U S A*. 2004; 101: 16745-9.

76. Lin MZ, McKeown MR, Ng HL, Aguilera TA, Shaner NC, Campbell RE, et al. Autofluorescent proteins with excitation in the optical window for intravital imaging in mammals. *Chem Biol.* 2009; 16: 1169-79.
77. Shcherbo D, Shemiakina II, Ryabova AV, Luker KE, Schmidt BT, Souslova EA, et al. Near-infrared fluorescent proteins. *Nat Methods.* 2010; 7: 827-9.
78. Chan MC, Karasawa S, Mizuno H, Bosanac I, Ho D, Prive GG, et al. Structural characterization of a blue chromoprotein and its yellow mutant from the sea anemone *Cnidopus japonicus*. *J Biol Chem.* 2006; 281: 37813-9.
79. Morozova KS, Piatkevich KD, Gould TJ, Zhang J, Bewersdorf J, Verkhusha VV. Far-red fluorescent protein excitable with red lasers for flow cytometry and superresolution STED nanoscopy. *Biophys J.* 2010; 99: L13-5.
80. Chapagain PP, Regmi CK, Castillo W. Fluorescent protein barrel fluctuations and oxygen diffusion pathways in mCherry. *J Chem Phys.* 2011; 135: 235101.
81. Shaner NC, Lin MZ, McKeown MR, Steinbach PA, Hazelwood KL, Davidson MW, et al. Improving the photostability of bright monomeric orange and red fluorescent proteins. *Nat Methods.* 2008; 5: 545-51.
82. Piatkevich KD, Subach FV, Verkhusha VV. Engineering of bacterial phytochromes for near-infrared imaging, sensing, and light-control in mammals. *Chem Soc Rev.* 2013; 42: 3441-52.
83. Krumholz A, Shcherbakova DM, Xia J, Wang LV, Verkhusha VV. Multicontrast photoacoustic in vivo imaging using near-infrared fluorescent proteins. *Sci Rep.* 2014; 4: 3939.
84. Yu D, Baird MA, Allen JR, Howe ES, Klassen MP, Reade A, et al. A naturally monomeric infrared fluorescent protein for protein labeling in vivo. *Nat Methods.* 2015; 12: 763-5.
85. Xia J, Pelivanov I, Wei C, Hu X, Gao X, O'Donnell M. Suppression of background signal in magnetomotive photoacoustic imaging of magnetic microspheres mimicking targeted cells. *J Biomed Opt.* 2012; 17: 061224.
86. Shu X, Royant A, Lin MZ, Aguilera TA, Lev-Ram V, Steinbach PA, et al. Mammalian expression of infrared fluorescent proteins engineered from a bacterial phytochrome. *Science.* 2009; 324: 804-7.
87. Auldridge ME, Satyshur KA, Anstrom DM, Forest KT. Structure-guided engineering enhances a phytochrome-based infrared fluorescent protein. *J Biol Chem.* 2012; 287: 7000-9.
88. Bhattacharya S, Auldridge ME, Lehtivuori H, Ihalainen JA, Forest KT. Origins of fluorescence in evolved bacteriophytochromes. *J Biol Chem.* 2014; 289: 32144-52.
89. Yu D, Gustafson WC, Han C, Lafaye C, Noirclerc-Savoye M, Ge WP, et al. An improved monomeric infrared fluorescent protein for neuronal and tumour brain imaging. *Nat Commun.* 2014; 5: 3626.
90. Shcherbakova DM, Verkhusha VV. Near-infrared fluorescent proteins for multicolor in vivo imaging. *Nat Methods.* 2013; 10: 751-4.
91. Stepanenko OV, Baloban M, Bublikov GS, Shcherbakova DM, Stepanenko OV, Turoverov KK, et al. Allosteric effects of chromophore interaction with dimeric near-infrared fluorescent proteins engineered from bacterial phytochromes. *Sci Rep.* 2016; 6: 18750.
92. Yu D, Dong Z, Gustafson WC, Ruiz-Gonzalez R, Signor L, Marzocca F, et al. Rational design of a monomeric and photostable far-red fluorescent protein for fluorescence imaging in vivo. *Protein Sci.* 2016; 25: 308-15.
93. Rumyantsev KA, Shcherbakova DM, Zakharova NI, Emelianov AV, Turoverov KK, Verkhusha VV. Minimal domain of bacterial phytochrome required for chromophore binding and fluorescence. *Sci Rep.* 2015; 5: 18348.
94. Shcherbakova DM, Baloban M, Pletnev S, Malashkevich VN, Xiao H, Dauter Z, et al. Molecular Basis of Spectral Diversity in Near-Infrared Phytochrome-Based Fluorescent Proteins. *Chem Biol.* 2015; 22: 1540-51.
95. Yuan C, Li HZ, Tang K, Gartner W, Scheer H, Zhou M, et al. Near infrared fluorescent biliproteins generated from bacteriophytochrome AphB of *Nostoc* sp. PCC 7120. *Photochem Photobiol Sci.* 2016.
96. Adam V, Berardozzi R, Byrdin M, Bourgeois D. Phototransformable fluorescent proteins: Future challenges. *Curr Opin Chem Biol.* 2014; 20: 92-102.
97. Stiel AC, Dean-Ben XL, Jiang Y, Ntziachristos V, Razansky D, Westmeyer GG. High-contrast imaging of reversibly switchable fluorescent proteins via temporally unmixed multispectral optoacoustic tomography. *Opt Lett.* 2015; 40: 367-70.
98. Amer MH. Gene therapy for cancer: present status and future perspective. *Mol Cell Ther.* 2014; 2: 27.
99. Bayer CL, Luke GP, Emelianov SY. Photoacoustic Imaging for Medical Diagnostics. *Acoust Today.* 2012; 8: 15-23.
100. Laufer J, Norris F, Cleary J, Zhang E, Treeby B, Cox B, et al. In vivo photoacoustic imaging of mouse embryos. *J Biomed Opt.* 2012; 17: 061220.
101. Liu Y, Kang N, Lv J, Zhou Z, Zhao Q, Ma L, et al. Deep Photoacoustic/Luminescence/Magnetic Resonance Multimodal Imaging in Living Subjects Using High-Efficiency Upconversion Nanocomposites. *Advanced Materials.* 2016.
102. Flores SC, Bernauer J, Shin S, Zhou R, Huang X. Multiscale modeling of macromolecular biosystems. *Brief Bioinform.* 2012; 13: 395-405.
103. Wang Y, Xia J, Wang LV. Deep-tissue photoacoustic tomography of Forster resonance energy transfer. *J Biomed Opt.* 2013; 18: 101316.
104. Wang Y, Wang LV. Forster resonance energy transfer photoacoustic microscopy. *J Biomed Opt.* 2012; 17: 086007.
105. Sample V, Mehta S, Zhang J. Genetically encoded molecular probes to visualize and perturb signaling dynamics in living biological systems. *J Cell Sci.* 2014; 127: 1151-60.
106. Kerppola TK. Visualization of molecular interactions using bimolecular fluorescence complementation analysis: characteristics of protein fragment complementation. *Chem Soc Rev.* 2009; 38: 2876-86.
107. To TL, Piggott BJ, Makhijani K, Yu D, Jan YN, Shu X. Rationally designed fluorogenic protease reporter visualizes spatiotemporal dynamics of apoptosis in vivo. *Proc Natl Acad Sci U S A.* 2015; 112: 3338-43.
108. Zlobovskaya OA, Sergeeva TF, Shirmanova MV, Dudenkova VV, Sharonov GV, Zagaynova EV, et al. Genetically encoded far-red fluorescent sensors for caspase-3 activity. *Biotechniques.* 2016; 60: 62-8.
109. Filonov GS, Verkhusha VV. A near-infrared BiFC reporter for in vivo imaging of protein-protein interactions. *Chem Biol.* 2013; 20: 1078-86.
110. Devor A, Bandettini PA, Boas DA, Bower JM, Buxton RB, Cohen LB, et al. The challenge of connecting the dots in the B.R.A.I.N. *Neuron.* 2013; 80: 270-4.
111. Zhou M, Li Q, Wang R. Current Experimental Methods for Characterizing Protein-Protein Interactions. *ChemMedChem.* 2016.